Shape matters in protein mobility within membranes

François Quemeneur[a,b,c,d], Jon K. Sigurdsson[e], Marianne Renner[f,g], Paul J. Atzberger[e,1], Patricia Bassereau[a,b,c,d,1], and David Lacoste[d,h,i,1,2]

[a]Institut Curie, Centre de Recherche, F-75248 Paris, France; [b]Centre National de la Recherche Scientifique, Unité Mixte de Recherche 168, F-75248 Paris, France; [c]Université Pierre et Marie Curie, F-75252 Paris, France; [d]CelTisPhyBio Laboratory of Excellence and Paris Sciences et Lettres, F-75005 Paris, France; [e]Department of Mathematics, University of California, Santa Barbara, CA 93106; [f]Biologie Cellulaire de la Synapse, Institut de Biologie Ecole Normale Supérieure, F-75005 Paris, France; [g]Institut National de la Santé et de la Recherche Médicale Unité 1024, F-75005 Paris, France; [h]Laboratoire de Physico-Chimie Théorique, Ecole Supérieure de Physique et Chimie Industrielles, F-75231 Paris, France; and [i]Centre National de la Recherche Scientifique, Unité Mixte de Recherche 7083, F-75231 Paris, France

The lateral mobility of proteins within cell membranes is usually thought to be dependent on their size and modulated by local heterogeneities of the membrane. Experiments using single-particle tracking on reconstituted membranes demonstrate that protein diffusion is significantly influenced by the interplay of membrane curvature, membrane tension, and protein shape. We find that the curvature-coupled voltage-gated potassium channel (KvAP) undergoes a significant increase in protein mobility under tension, whereas the mobility of the curvature-neutral water channel aquaporin 0 (AQP0) is insensitive to it. Such observations are well explained in terms of an effective friction coefficient of the protein induced by the local membrane deformation.

Brownian motion | Saffman–Delbrück | internal membrane structure | drag force | micropipette aspiration

Brownian motion plays an essential role in biological processes. Since the pioneering experiments of Perrin (1), the observation of diffusing objects has emerged as a mean to extract the rheological properties of the surrounding medium or the probe particle size. The theoretical investigation of diffusion of proteins within membranes has been studied widely going back to P. G. Saffman and M. Delbrück (SD). They investigated the hydrodynamic drag acting on a membrane inclusion when the membrane is described as a 2D fluid sheet of viscosity μ_m embedded within a less viscous fluid of viscosity η (2). In this theory, the diffusion coefficient D_0 in the limit of a large viscosity contrast between the membrane and bulk fluid is given by:

$$D_0 = \frac{k_B T}{4\pi\mu_m}\left[\log\left(\frac{\ell}{a_p}\right) - \gamma\right].\qquad [1]$$

The length $\ell = \mu_m/\eta$ is the length scale over which flow is generated within the bilayer by the inclusion, $k_B T$ is the thermal energy, and γ is Euler's constant. This model predicts a logarithmic dependence of D_0 on the protein radius a_p, which has been confirmed for some in vitro experiments on membranes containing transmembrane proteins (see ref. 3 and references therein). In contrast, the experiments of Gambin et al. (4) showed significant deviations from the SD theory.

A possible origin for the discrepancy observed by Gambin et al. (4) is the significant local membrane deformation due to the interaction between the inclusion and the lipid bilayer (5). Naji et al. suggested in ref. 6 that inclusions experience additional dissipation, either due to internal flows within the membrane or to additional fluid flows produced by the deformed membrane. This work triggered a number of theoretical studies investigating the coupling of inclusion proteins with the membrane that had been pioneered by the Seifert's group (see ref. 7 and references therein). Such studies have systematically gone beyond the SD model by including additional effects (8–12). So far, a thorough verification of these ideas has not been attempted. To investigate the effect of the protein–lipid coupling on the protein mobility, we study its dependence on membrane tension, because this parameter affects the local membrane deformation.

In this work, we compare the mobility of two transmembrane proteins with the same lateral size, aquaporin 0 (AQP0) and a voltage-gated potassium channel (KvAP), reconstituted in giant unilamellar vesicles (GUVs). Whereas AQP0 does not deform locally the bilayer, KvAP locally bends the membrane (13). Using single-particle tracking (SPT), we demonstrate that the curvature-coupled protein KvAP undergoes a significant increase in mobility under tension, whereas the mobility of the curvature-neutral water channel AQP0 is insensitive to it. This difference, which goes beyond the SD model, is explained by an approach that includes the interplay between membrane deformation and friction with the surrounding medium and within the bilayer. This is compelling evidence that the Brownian motion of a shaping-membrane protein is not simply dependent on the inclusion size but also related to the lateral extension of the deformed membrane patch, which depends on tension.

Results

The membrane inclusions are two tetrameric transmembrane proteins of size $a_p = 4$ nm: (*i*) AQP0, a water channel abundant in the eye lens (14), and (*ii*) an archeabacterial voltage-gated potassium channel (KvAP) (15). KvAP has been shown to have a strong affinity for curved membranes and thus inducing bending of the membrane. The inclusion ability to curve membranes is

---

Significance

Lateral Brownian diffusion of proteins in lipid membranes has been predicted by Saffman and Delbrück to depend only on protein size and on the viscosity of the membrane and of the surrounding medium. Using a single-molecule tracking technique on two transmembrane proteins that bend the membrane differently and are reconstituted in giant unilamellar vesicles, we show that the mobility of a membrane protein is crucially dependent on the local membrane deformation self-generated around the protein, which can be tuned by adjusting membrane tension. The feedback between membrane shaping and mobility is well explained by analytical and numerical models that include the friction of the deformed membrane patch with the surrounding medium and the friction internal to the bilayer.

generally quantified by its spontaneous curvature C_p, which reflects the preferred value of local membrane curvature. For KvAP, we have measured $C_p = 0.04$ nm^{-1} (13). In contrast, AQP0 does not exhibit any preference for curved membranes, and thus has a zero spontaneous curvature (13). To investigate the lateral mobility of these proteins in membranes, they were reconstituted at low density ($\sim$40 inclusions per μm^2) in fluid phase GUVs, and a small protein fraction was then labeled with quantum dots (QDs). Although both protein insertions are present in the GUV, only one insertion was labeled with the QDs (13). Micropipette aspiration was then used to hold the GUV in place and to control its membrane tension Σ (16) (Fig. 1A). To measure protein displacements, the QD position was detected with SPT near the bottom of the vesicle using epifluorescence microscopy equipped with a fast and sensitive camera (17). We limited our analysis to a small rectangular membrane area (Fig. 1B). We find that the mean-square displacement (MSD) of the proteins exhibits a linear time dependence at short time and a crossover to a constant value dependent on the size of the observation window at larger time (*Materials and Methods* and Fig. S1). Details of our protocols and analysis are described in the *Supporting Information*.

We determined the diffusion coefficient D_{eff} for each applied membrane tension (Fig. 2 and Fig. S2). In the high-tension limit, the diffusion coefficients of AQP0 and KvAP are comparable and correspond to the value predicted by the SD model (Eq. 1), namely $D_0 = 2.5$ μm^2/s for $a_p = 4$ nm. When the tension drops from 10^{-3} to 10^{-6} N/m, less than a 5% variation of D_{eff} is found for AQP0, whereas a drastic decrease of about 40% is revealed for KvAP. In any case, such a tension dependence is incompatible with the standard SD approach.

Fig. 1. Experimental approach to diffusion measurements in fluctuating membrane. (*A*) Schematic of experimental setup: a GUV containing tracer molecule (lipid, AQP0, or KvAP) labeled with a QD is aspirated in a micropipette. In a typical sequence, 100–1,000 individual QDs explore the bottom pole of the GUV. Single QD displacements are measured as a function of the applied membrane tension Σ. (*B*) Example of QD trajectory. The truncated circle corresponds to the boundary of the area explored by QDs within the depth of field of the microscope. Only the green part of the trajectory contained in a centered square region of interest is considered for the single-QD tracking analysis. One pixel is 160 nm.

Fig. 2. Protein lateral mobility in fluctuating membranes. Semilogarithmic plot of the diffusion coefficients (D_{eff}) as a function of the membrane tension Σ, for AQP0 (◆) and KvAP (▲) labeled with streptavidin QDs. Each point represents a median diffusion coefficient obtained from hundreds of individual trajectories for a GUV at a given tension; the error bars correspond to SE. KvAP data adjusted by Eq. 3 (solid line) yields a protein coupling coefficient $\Theta = 3.5 \times 10^{-7}$ m considering $a = 5$ nm, $\kappa = 20$ k_BT and $D_0 \simeq 2.5$ μm^2/s. Simulations of the protein diffusion on a membrane subject to thermal fluctuations (■) agree well with the experimental data and theory. (*Insets*) Sketches of membrane deformation near proteins.

To address this issue, we have developed an analytical model and numerical simulations. SD theory implicitly assumes that the protein diffuses in a membrane that remains flat and unaffected by the presence of the protein. In contrast, we take into account that the protein strongly affects its environment. The back action on the diffusing object, translates into a modified drag force. This phenomenon is general in physics and is known as polaron effect (18). A polaron is a charge carrier that deforms a surrounding lattice and moves in it with an induced polarization field. Similarly in liquids, an isolated ion recruits nearby counterions in a process that affects its mobility. Here, we consider a single protein diffusing on a membrane patch of size $L \gg a_p$ described by a height function $h(\mathbf{r})$. We use the modified Helfrich Hamiltonian:

$$\mathcal{H}_0[h, \mathbf{R}] = \frac{\kappa}{2} \int d^2\mathbf{r} \left[\left(\nabla^2 h\right)^2 + \frac{\Sigma}{\kappa}(\nabla h)^2 - \Theta G(\mathbf{r} - \mathbf{R})\nabla^2 h \right], \quad [2]$$

where the first two terms represent the energy of elastic bending of the bilayer with modulus κ and tension Σ, and the last term models the membrane curvature induced at the location of the protein $\mathbf{R}$, which is time dependent. The strength of the induced curvature scales linearly with the protein spontaneous curvature C_p, $\Theta = 4\pi a_p^2 C_p$, similarly to refs. 6 and 8. The range of influence of the protein on the membrane is modeled by the weight function G, which is normalized to 1 and is nonzero over a distance of the order of a_p. This Hamiltonian carries with it a cutoff length a, which corresponds to the bilayer thickness ($\sim$5 nm). From this approach, we obtain the membrane profile around the inclusion given in Eq. S37. The lateral characteristic width of this membrane profile is the crossover length between the tension and the bending regime for the fluctuations, namely $\xi = \sqrt{\kappa/\Sigma}$, whereas the characteristic height of the membrane deformation at zero tension scales as Θ (Eq. S31). The geometry of the local deformation from the membrane midplane induced by KvAP when subjected to various tensions is shown in Fig. 3 (Fig. S3). Using the method of refs. 6, 8, and 10, we have carried out simulations (with parameters shown in Fig. S4), which also confirm the expected theoretical membrane profile as shown in Fig. 3.
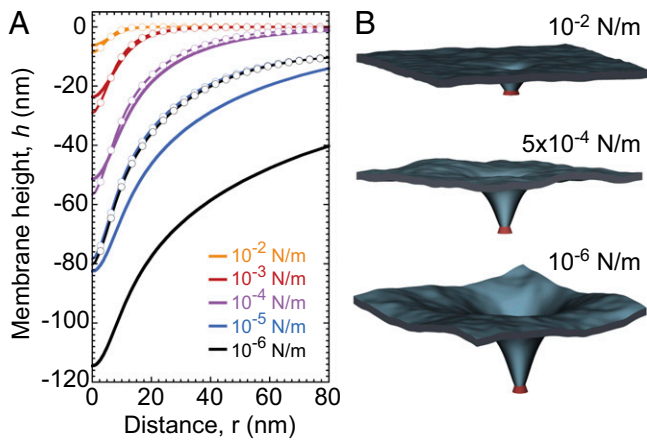
Fig. 3. Membrane shape as a function of the tension. (*A*) Profile calculated from Eq. S37 with $\Theta = 3.5 \times 10^{-7}$ m, $\kappa = 20\, k_B T$, and $a_p = 4$ nm (solid lines). Profile calculated from the numerical energy minimum shape using simulation (dashed line). The height value far away from the inclusion is chosen to be zero. Discrepancy at low tension originates from the finite size of the membrane L^2 used in the simulations (*Supporting Information*). (*B*) Three-dimensional membrane profiles obtained from numerical simulations for three different tensions (see also Movies S1 and S2).

Below, we investigate the implications of this local membrane deformation for the mobility of the protein. The model assumes that the dynamics of the membrane is controlled by hydrodynamics in the surrounding fluid of viscosity η. The corresponding timescale is much faster than the diffusion time of the inclusion, justifying the use of an adiabatic approximation to derive an effective dynamics for the protein. Using the framework developed by Démery and co-worker in ref. 9, the effective drag force exerted on the inclusion, namely, $\bar{\mathbf{f}} = -\nabla_R \mathcal{H}_0[h, \mathbf{R}]$, can be obtained analytically at fixed inclusion velocity $\mathbf{v}$. To leading order in $\mathbf{v}$, this leads to a friction coefficient λ given by $\bar{\mathbf{f}} = -\lambda\mathbf{v}$. We find that $\lambda(\sigma) = \Theta^2 \eta W_0(\sigma)/2a$, where $\sigma = \Sigma a^2/4\pi\kappa$ is a reduced tension and $W_0(\sigma)$ is a function given in Eq. S27. The diffusion coefficient D_{eff} is obtained from the effective drag coefficient using the Einstein relation:

$$\frac{D_0}{D_{eff}} = 1 + \frac{\eta D_0 \Theta^2 W_0(\sigma)}{2a k_B T},\qquad \textbf{[3]}$$

where D_0 represents the bare diffusion coefficient of the inclusion in a flat tense membrane, given by Eq. **1**. The tension dependence of D_{eff} is shown in Fig. 2 and Fig. S5. The same dependence was found in simulations (Fig. 2 and Movies S1 and S2), in which the protein diffusivity was directly computed from the MSD of stochastic trajectories. Moreover, it is important to appreciate that the friction coefficient λ is independent of temperature, which shows that the thermal fluctuations of the membrane do not contribute to this effect within the adiabatic approximation. An extended description of the theory and simulations is proposed in the *Supporting Information*.

Discussion

We next test our model against the KvAP experiments. We find that theory and simulations fit very well the experimental results for D_{eff} versus Σ using a coupling coefficient $\Theta = 3.5 \times 10^{-7}$ m. This proves that the mechanical coupling between the proteins and the membrane can strongly affect protein mobility. At high tension, the experimental data of AQP0 and KvAP converge to the same plateau value, consistently with the SD limit because they have about the same steric radius. As a control, we measured the diffusion coefficient of pure lipids, and confirmed that

it is independent of tension as found for AQP0 (Fig. S6). The corresponding constant value for D_0 agrees with the prediction of the SD model, using a lipid size $a_p = 0.5$ nm. At lower tension, Fig. 2 shows that the KvAP data start to deviate significantly from the plateau at $\Sigma \sim 5 \times 10^{-3}$ N/m, which corresponds to the point at which the lateral characteristic length ξ is of the order of the protein size as expected from our theory.

An additional outcome of this approach concerns the dependence of D_{eff} with the protein radius a_p, which can be obtained from the following scaling argument. Because the protein makes a fixed angle with respect to the membrane, $C_p \sim 1/a_p$. Given the relation $\Theta = 4\pi a_p^2 C_p$, this implies $\Theta \sim a_p$. Below the crossover to the SD regime, the local membrane deformation is much larger than the protein size $a_p \ll \xi$, and the drag is dominated by the contribution due to the membrane deformation. Therefore, using Eq. **3**, one finds $D_{eff} \sim k_B Ta/a_p^2$, in agreement with ref. 9. Note that such a result is also compatible with the Stokes–Einstein scaling law in $1/a_p$ obtained in ref. 6, because in this reference only one characteristic length for the protein is used; thus, $a \simeq a_p$.

Contribution of an Advected Lipid Layer. Despite a good agreement between model and data, the physical interpretation of the coupling coefficient Θ requires a more detailed discussion. Indeed, the spontaneous curvature deduced from this coupling coefficient via a fit of the data is significantly larger than that obtained from thermodynamic measurements, based on the preferential sorting at equilibrium of the proteins between GUV and highly curved membrane nanotubes (13). One possible interpretation for this discrepancy is that, in dynamic measurements, the basic relevant object, namely, the association of the moving protein with the deformed membrane around it, may have a size larger than a_p. Such an enhancement of the size could describe physically a layer of lipids dragged by the motion of the protein as considered in ref. 11. Given the value of the coupling coefficient Θ, we obtain an effective area of the protein of the order of 2,200 nm². This is equivalent to an effective radius of 47 nm, a rather large value with respect to the lipid and protein sizes (0.5 and 4 nm, respectively).

Additional Contribution Due to Interleaflet Friction. At this point, we propose an alternate explanation for the discrepancy between the dynamic measurement and the thermodynamic one. In the approach outlined so far, the dissipation only originates in the fluid displaced by the "bump" in the membrane. However, as pointed out in ref. 6, other dissipation mechanisms in the membrane are possible and likely to be dominant in highly viscous membranes. As a consequence of the curvature induced in the bilayer near the protein, a difference of lipid density between the leaflets is built up, which either relaxes after the protein has passed or is carried by the protein. In any case, there is locally a difference of velocity between each leaflet, which is responsible for further dissipation from intermonolayer slip as the inclusion moves.

A simplified internal structure can be given to the membrane by decorating both leaflets with additional fields representing lipid density deviations from the equilibrium density, $\rho^\pm$ (19). A neutral surface is defined for each leaflet by the property that bending and stretching are decoupled in energy when deformations are defined with respect to it. The neutral surfaces of each monolayer are located at a distance d from the overall neutral surface of the bilayer. Deviations from the equilibrium density for each layer can be accounted for with the Hamiltonian:

$$\mathcal{H}[h, \mathbf{R}] = \mathcal{H}_0[h, \mathbf{R}] + \frac{k^m}{2} \int_{L^2} d^2\mathbf{r}\left[(\rho^+ - 2dH)^2 + (\rho^- + 2dH)^2\right],\qquad \textbf{[4]}$$

where H represents the mean curvature of the membrane, and k^m is the elastic compression modulus of the 2D fluid within each monolayer.

As far as the dynamics is concerned, we introduce two additional parameters, namely, the shear viscosity of each lipid monolayer, μ_m, and the friction coefficient between the two leaflets, b. We find with this improved model the same stationary membrane profile but a modified drag coefficient of the form:

$$\lambda(\sigma) = \frac{\Theta^2 \eta}{2a}\left(W_0 + \frac{bd^2}{\eta a}W_1 + \frac{d^2}{a^2}W_2 + \frac{\mu_m d^2}{2\eta a^3}W_3\right), \qquad [5]$$

where W_i are functions dependent on the reduced tension σ, defined in the *Supporting Information* (Eq. S46).

This drag friction coefficient reflects three dissipation sources: (*i*) the dissipation in the bulk fluid, which is proportional to η and corresponds to the W_0 term discussed above in Eq. **3** with a correction given by the W_2 term, (*ii*) the interleaflet dissipation, which is proportional to b and appears in the W_1 term, and (*iii*) the dissipation due to the shear viscosity of a single monolayer, which is proportional to μ_m and is given by the W_3 term. One can evaluate the relative importance of these contributions in Eq. **5** using the following bilayer parameters $a = 5$ nm, $d = 1$ nm (19), $b = 10^9$ J·s·m^{-4} (20–22) and $\mu_m = 6 \times 10^{-10}$ J·s·m^{-2} (23), from which one finds the dimensionless factors $bd^2/\eta a \simeq 200$, $(d/a)^2 \simeq 0.04$, and $\mu_m d^2/2\eta a^3 \simeq 2$. It follows from such estimates that the monolayer friction should play the largest role in the effective friction of the protein (Eq. **5**). As a result, it should also be the case for the effective diffusion coefficient corresponding to this drag coefficient $\lambda(\sigma)$:

$$\frac{D_0}{D_{eff}} = 1 + \frac{D_0 \lambda(\sigma)}{k_B T}. \qquad [6]$$

With the inclusion of dissipative mechanisms internal to the membrane, we can still account for the dependence of D_{eff} versus Σ (Fig. S6) and Eq. **6**, but with a lower a coupling coefficient $\Theta = 3.4 \times 10^{-8}$ m, corresponding to a $C_p = 0.16$ nm^{-1}. This value is then much more compatible with the thermodynamic measurements previously reported in ref. 13.

In this paper, we provide compelling evidence that the effective mobility of a protein is controlled not only by its intrinsic geometric size as in the SD model, but by an effective size that depends on dissipation mechanisms present in the surrounding fluid and in the membrane. An additional outcome of our study is that it is possible to extract from this type of experiment a measurement of the spontaneous curvature of the protein and of the interleaflet friction at the single-molecule level. All these parameters depend on the local environment and on the shape of the protein, in a way that needs to be investigated more systematically in future experiments.

In cell membranes, the local environment of proteins is heterogeneous and dynamic. A more realistic approach to such a situation would require further studies on (*i*) the diffusion of a protein in a membrane that may be driven out of equilibrium (24), or (*ii*) the diffusion of a protein that can be activated, such as voltage-gating channels, mechanosensitive channels, G-protein–coupled receptors or light-activated rhodopsins. The strong dependence of the protein mobility on its local environment should lead to a more complex kinetics of clustering of membrane receptors and of association of membrane receptors to ligands. More generally, such effects can contribute to the lateral organization of cell membranes and to the formation of dynamical heterogeneities.

Materials and Methods

Detailed protocols are given in *SI Materials and Methods*.

Protein Reconstitution in GUVs and Micromanipulation. Archeabacterial voltage-gated potassium channels (KvAP) or native AQP0 were reconstituted in GUVs using the electroformation method on platinum wires (13, 25, 26). The final protein-to-lipid mass ratio is estimated to 1:200, corresponding approximately to 40 proteins per μm^2. Before the SPT experiments, biotinylated proteins were labeled with QD655–streptavidin conjugate (Life Technologies). QD-labeled GUVs were then transferred to the microscopy observation chamber. They were aspirated in a glass micropipette and the membrane tension Σ was adjusted by changing the difference of hydrostatic pressure (16). For each vesicle, the membrane was prestressed at $\Sigma \approx 10^{-3}$ N/m during 2 min and then Σ was decreased to the lowest value before diffusion measurement.

QD Imaging and Analysis. Micromanipulated GUV was positioned so that the bottom pole could sit within the depth of field of the optical Nikon Eclipse Ti microscope (Fig. 1*A*). The high-speed imaging of single QDs attached to tracer molecules was made using an epifluorescence microscope equipped with an electron-multiplying CCD camera (iXon DU-897; Andor Technology). The membrane tension was then increased step by step and for each membrane tension, two sequences of 30,000 images were recorded with 2-ms exposure time. In a typical sequence, 100–1,000 individual QDs explore a membrane surface of 3- to 5-μm width in the focal plane (Fig. 1*B*). Detection and tracking of individual QDs was performed with MATLAB routines (SPTrack, version 4). QD centroid positions were determined with a spatial resolution of 10 nm. Trajectories were built by connecting the fluorescence peaks that could be unequivocally assigned to individual QD using a modified routine of the Multiple-Target Tracing (MTT) software developed by Sergé et al. (27), based on Bayesian inference methods. To avoid geometrical artifacts related to the projection of these 3D trajectories on the focal plane, we limited our analysis to a square region of interest (ROI) around the GUV bottom pole. Only trajectories that were at least 30 points long in ROI were kept for further analysis.

For each vesicle at a given membrane tension, we recorded between 50–1,000 trajectories in ROI. The diffusion coefficient of the tracer is extracted from the analysis of the MSD, $\langle \Delta r^2(t) \rangle$ defined in Eq. S1. Although the MSD appears linear with respect to time at short time, a saturation at larger time is typically observed. We interpret this saturation illustrated in Fig. S1 as a consequence of the truncation of the trajectories, which leave the observation window (the ROI). A theory based on the solution of the diffusion equation in a finite 2D domain of size $(L_x \times L_y)$, developed in the *Supporting Information*, gives the conditional MSD to remain in this window: $\langle \Delta r^2(t) \rangle_{cond} \to 0.0947(L_x^2 + L_y^2)$, for $t \to \infty$. This explains the crossover between a linear behavior of the MSD at short times to a plateau at long times. In all experiments, we have carefully checked that we were far from the crossover regime when measuring the effective mobility. We particularly thank M. Lomholt (MEMPHYS, Odense, Denmark) for insightful discussions on this issue.

This diffusion coefficient was obtained from the short time behavior of the MSD with $\langle \Delta r^2(t) \rangle = 4Dt + b$, where b is a variable offset reflecting the spot localization accuracy (28). From this analysis, we obtained a distribution of diffusion coefficients corresponding to one vesicle at one tension from which we extracted the median value and the SE of the diffusion coefficient reported in Fig. 2.

Computational Methods. The computational methods follow closely the algorithms developed in ref. 10. The membrane–protein system were thermalized by introducing stochastic driving fields for both the proteins and membrane. The stochastic dynamic equations were integrated in time using the Euler–Maruyama method (29). The membrane profiles were extracted from our computational model by allowing for the membrane mechanics to relax to equilibrium for a fixed protein and taking a cross-section through the protein location. To obtain statistics, we used a straightforward Monte Carlo approach, where independent trajectories were realized for the protein diffusion subjected to membrane thermal fluctuations. The tension dependence of the diffusivity was determined from simulations of the membrane–protein system started with a flat membrane and letting the system equilibrate. After equilibration, the MSD was computed and the diffusivity statistics determined by generating several simulation trajectories for each reported tension value. In this manner, both the energy minimizing shape profiles and stochastic protein dynamics were obtained from the computational model.

1. Perrin JB (1909) Mouvement brownien et réalité moléculaire. *Ann Chim Phys* 19: 5–104.
2. Saffman PG, Delbrück M (1975) Brownian motion in biological membranes. *Proc Natl Acad Sci USA* 72(8):3111–3113.
3. Ramadurai S, et al. (2009) Lateral diffusion of membrane proteins. *J Am Chem Soc* 131(35):12650–12656.
4. Gambin Y, et al. (2006) Lateral mobility of proteins in liquid membranes revisited. *Proc Natl Acad Sci USA* 103(7):2098–2102.
5. Phillips R, Ursell T, Wiggins P, Sens P (2009) Emerging roles for lipids in shaping membrane-protein function. *Nature* 459(7245):379–385.
6. Naji A, Levine AJ, Pincus PA (2007) Corrections to the Saffman-Delbruck mobility for membrane bound proteins. *Biophys J* 93(11):L49–L51.
7. Reister-Gottfried E, Leitenberger SM, Seifert U (2010) Diffusing proteins on a fluctuating membrane: Analytical theory and simulations. *Phys Rev E Stat Nonlin Soft Matter Phys* 81:031903.
8. Naji A, Atzberger PJ, Brown FL (2009) Hybrid elastic and discrete-particle approach to biomembrane dynamics with application to the mobility of curved integral membrane proteins. *Phys Rev Lett* 102(13):138102.
9. Démery V, Dean DS (2010) Drag forces in classical fields. *Phys Rev Lett* 104(8):080601.
10. Sigurdsson JK, Brown FLK, Atzberger PJ (2013) Hybrid continuum-particle method for fluctuating lipid bilayer membranes with diffusing protein inclusions. *J Comput Phys* 252:65–85.
11. Camley BA, Brown FLH (2012) Contributions to membrane-embedded-protein diffusion beyond hydrodynamic theories. *Phys Rev E Stat Nonlin Soft Matter Phys* 85:061921.
12. Komura S, Ramachandran S, Seki K (2012) Anomalous lateral diffusion in a viscous membrane surrounded by viscoelastic media. *Europhys Lett* 97(6):68007.
13. Aimon S, et al. (2014) Membrane shape modulates transmembrane protein distribution. *Dev Cell* 28(2):212–218.
14. Harries WEC, Akhavan D, Miercke LJ, Khademi S, Stroud RM (2004) The channel architecture of aquaporin 0 at a 2.2-A resolution. *Proc Natl Acad Sci USA* 101(39):14045–14050.
15. Lee S-Y, Lee A, Chen J, MacKinnon R (2005) Structure of the KvAP voltage-dependent K$^+$ channel and its dependence on the lipid membrane. *Proc Natl Acad Sci USA* 102(43):15441–15446.
16. Evans E, Rawicz W (1990) Entropy-driven tension and bending elasticity in condensed-fluid membranes. *Phys Rev Lett* 64(17):2094–2097.
17. Domanov YA, et al. (2011) Mobility in geometrically confined membranes. *Proc Natl Acad Sci USA* 108(31):12605–12610.
18. Landau LD (1933) Über die Bewegung der Elektronen in Kristalgitter. *Phys Z Sowjetunion* 3:644645.
19. Seifert U (1997) Configurations of fluid membranes and vesicles. *Adv Phys* 46(1):13–137.
20. Fournier J-B, Khalifat N, Puff N, Angelova MI (2009) Chemically triggered ejection of membrane tubules controlled by intermonolayer friction. *Phys Rev Lett* 102(1):018102.
21. Rodríguez-García R, et al. (2009) Bimodal spectrum for the curvature fluctuations of bilayer vesicles: Pure bending plus hybrid curvature-dilation modes. *Phys Rev Lett* 102(12):128101.
22. Horner A, Akimov SA, Pohl P (2013) Long and short lipid molecules experience the same interleaflet drag in lipid bilayers. *Phys Rev Lett* 110(26):268101.
23. Vaz WLC, Goodsaid-Zalduondo F, Jacobson K (1984) Lateral diffusion of lipids and proteins in bilayer membranes. *FEBS Lett* 174(2):199–207.
24. Lacoste D, Bassereau P (2014) *An Update on Active Membrane* (CRC Press, Taylor and Francis Group, Abingdon, UK), pp 271–287.
25. Aimon S, et al. (2011) Functional reconstitution of a voltage-gated potassium channel in giant unilamellar vesicles. *PLoS One* 6(10):e25529.
26. Berthaud A, Manzi J, Pérez J, Mangenot S (2012) Modeling detergent organization around aquaporin-0 using small-angle X-ray scattering. *J Am Chem Soc* 134(24):10080–10088.
27. Sergé A, Bertaux N, Rigneault H, Marguet D (2008) Dynamic multiple-target tracing to probe spatiotemporal cartography of cell membranes. *Nat Methods* 5(8):687–694.
28. Michalet X (2010) Mean square displacement analysis of single-particle trajectories with localization error: Brownian motion in an isotropic medium. *Phys Rev E Stat Nonlin Soft Matter Phys* 82(4 Pt 1):041914.
29. Kloeden PE, Platen E (1992) *Numerical Solution of Stochastic Differential Equations* (Springer, Berlin).

APPLIED PHYSICAL SCIENCES

BIOPHYSICS AND COMPUTATIONAL BIOLOGY

Supporting Information

Quemeneur et al. 10.1073/pnas.1321054111

SI Materials and Methods

Lipids and Reagents. Chemicals were purchased from Sigma-Aldrich unless specified otherwise. Egg L-α-phosphatidic acid (EPA), egg L-α-phosphatidylcholine (EPC), and 1,2-distearoyl-*sn*-glycero-3-phosphoethanolamine-*N*-[biotinyl(polyethylene-glycol)-2000] [DSPE-PEG(2000)-biotin] were obtained from Avanti Polar Lipids. QD655–streptavidin conjugate were provided from Life Technologies. EZ-Link maleimide-PEG11-biotin was purchased from Pierce. Detergents, *n*-decyl-maltopyranoside (DM) and *n*-octyl-β-D-glucopyranoside (OG), were bought from Affymetrix.

Protein Purification and Reconstitution in Giant Unilamellar Vesicles. KvAP, an archeabacterial voltage-gated potassium channel (tetramer, 112 kDa), was overexpressed in *Escherichia coli* and purified as described in ref. 1 and reference therein. Bacteria were solubilized in DM, and then KvAP was purified using a poly-histidine-tag affinity column (HiTrap Ni-Sepharose; GE Healthcare) followed by a size exclusion chromatography (Superdex200 10/300 GL; GE Healthcare). Native aquaporin 0 (AQP0) (tetramer, 112 kDa) was purified from sheep crystalline cortical lenses as reported in ref. 2. Cortical lens lipid membranes were isolated and then solubilized with OG. AQP0 were purified using an ion exchange column (Mono-S 5/50 GL; GE Healthcare) followed by a size exclusion chromatography (Superose12 10/300 GL; GE Healthcare). KvAP and AQP0 tetramers in detergent were then labeled with maleimide-PEG11-biotin. Protein purity and integrity were checked by SDS/polyacrylamide gel electrophoresis. Protein concentrations were determined by protein adsorbance at 280 nm (NanoDrop Spectrophotometer; Thermo Scientific). Labeled proteins were then mixed with small unilamellar vesicles (SUVs) of EPC and EPA (9:1 molar ratio) presolubilized with detergent (i.e., 10 mM DM for KvAP and 31 mM OG for AQP0) (3). The free labeling molecules and detergent were removed by dialysis. The final SUV concentration was ~10 mg/mL in a relatively low-salt buffer (5 mM KCl, 1 mM Hepes, pH 7.4) with a protein-to-lipid mass ratio of 1:10. Suspensions of SUV-containing proteins were flash-frozen in liquid nitrogen and kept until use at −80 °C.

KvAP or AQP0 reconstitution in giant unilamellar vesicles (GUVs) was performed using the electroformation protocol on platinum wires as described in ref. 4. SUVs containing proteins were mixed with pure EPC/EPA SUVs to achieve a final protein-to-lipid mass ratio of 1:200, corresponding to ~40 proteins per μm². Droplets of the SUV solution were deposited onto two parallel platinum wires and partially dehydrated at room pressure and humidity for 1 h. Lipid–protein films were then rehydrated in a solution containing 5 mM KCl, 5 mM Hepes, and 385 mM sucrose at pH 7.4, while keeping the platinum wires (diameter, 0.5 mm; edge-to-edge distance, 2 mm; Goodfellows) under sinusoidal voltage of 1 V (peak-to-peak) at 10 Hz for 2 h maximum. The lipid-only GUVs were prepared using a lipid mixture in chloroform containing EPC/EPA in a 9:1 molar ratio, complemented with 0.01% of DSPE-PEG(2000)-biotin. It was deposited onto platinum wires and hydrated under an AC field as previously described.

Before the single-particle tracking (SPT) experiments, the GUV suspension was diluted with a buffer solution of matching osmolarity containing 10 mM Hepes, 5 mM KCl, 95 mM NaCl, ~175 mM glucose, and 25 mg/L β-casein at pH 7.4. A small amount (~10 pmol) of QD655–streptavidin conjugate was added. After 1- to 2-min incubation, the GUVs were washed with the same buffer solution four times for 90 s at 1,000 × *g* in a minicentrifuge. GUVs obtained with this protocol were spherical and presented no observable defects in the membrane (5).

Micromanipulation and Quantum Dot Imaging on GUV. Quantum dot (QD)-labeled GUVs were transferred to the microscopy observation chamber passivated with β-casein solution (1 g/L for 30 min). They were aspirated in a glass micropipette hold by a micromanipulator (Narishige) and a custom-made hydraulic system. The membrane tension Σ was determined using $\Sigma = (\Delta P\, R_{pip})/(2(1 - R_{pip}/R_{ves}))$, where R_{pip} is the inner pipette radius, R_{ves} is the vesicle radius, and ΔP is the difference of hydrostatic pressure caused by the vertical displacement of the water reservoir connected to the pipette (6). For each vesicle, membrane was prestressed at $\Sigma \approx 10^{-3}$ N/m during 2 min and Σ was decreased to the lowest value before diffusion measurement.

Micromanipulated GUV was positioned so that the bottom pole could sit within the depth of field of the optical microscope. The high-speed imaging of single QDs attached to tracer molecules (lipid or protein) was made using an epifluorescence microscope (Eclipse Ti; Nikon France SAS) equipped with a high-pressure Hg lamp as a light source, a Nikon Plan Fluor 100 oil-immersion objective (N.A. = 1.3), and a back-thinned electron-multiplying CCD camera (iXon DU-897; Andor Technology). The fluorescence filter set QD655 (BP435/40, dichroic 510 nm, BP655/15) was obtained from Semrock. The membrane tension was then increased step by step, and for each membrane tension, two sequences of 30,000 images were recorded with 2-ms exposure time and electron multiplication gain of 200. In a typical sequence, 100–1,000 individual QDs explore a membrane surface of 3- to 5-μm width in the focal plane.

We have estimated the viscous drag experienced by the QD as it moves through the aqueous solvent . With a QD655 radius of $R_{QD} = 10$ nm, we estimated the 3D diffusion coefficient of the QD using Stokes–Einstein equation, $D = (k_B T)/(6\pi\eta R_{QD}) \approx 21\ \mu m^2/s$. This value is six times larger than the lipid or protein diffusion coefficients reported in our works. This means that the effective viscous drag experienced by QD bound to a membrane component is dominated by the drag contribution associated to the lipid or protein moving through the membrane, in agreement with ref. 7.

SPT and Analysis. We use SPT, which has emerged as an alternative to fluorescence recovery after photobleaching, capable of characterizing the dynamics of single lipids and proteins at both short time and length scales. This overcomes population averaging effects and provides a level of resolution allowing for new mechanisms to be unraveled at the molecular scale in biological membranes.

Detection and tracking of individual QD was performed with MATLAB routines (SPTrack version 4), on the whole image sequences as illustrated in the *Inset* of Fig. 1*B*. Single QDs were identified by their blinking. Fluorescent peaks in each frame of the image sequence were found by fitting local maxima with a 2D Gaussian function corresponding to the point spread function of the experimental setup. Using this procedure, the peak intensity and the centroid position in the two lateral dimensions were determined with a spatial resolution of 10 nm. Weak or asymmetric peaks were discarded by applying appropriate thresholds. Trajectories were built by connecting the fluorescence peaks that could be unequivocally assigned to individual QD using a modified routine of the multiple-target tracing (MTT) software developed by Sergé et al. (8) based on Bayesian inference methods.

To avoid geometrical artifacts related to the projection of these 3D trajectories on the focal plane (tracers diffusing in membrane

with curvature of the order of 0.05–0.15 μm^{-1}), we limited our analysis to a small membrane area around the GUV bottom pole. The size of this square region of interest (ROI) was adjusted depending on the vesicle radius, such that the relative difference between the projected area and the apparent membrane cap surface remains lower than 0.5%. Only trajectories that were at least 30 points long in ROI were kept for further analysis (Fig. 1B). For each vesicle at a given membrane tension, we obtained between 50 and 1,000 trajectories in ROI. To determine diffusion coefficients, we calculated the mean-square displacement (MSD) from the QD displacements:

$$\langle \Delta r^2(n \cdot \delta t) \rangle = \frac{1}{N-n} \sum_{i=1}^{N-n} \left[(x_{i+n} - x_i)^2 + (y_{i+n} - y_i)^2 \right], \quad \text{[S1]}$$

where x_i and y_i are the coordinates of the QD in frame i, N is the total number of points in the trajectory, δt is the time interval between two consecutive frames, and $t = n \cdot \delta t$ is the time interval over which displacement is averaged. The diffusion coefficient D was calculated for individual trajectory by fitting the points 2–5 (point 1 being the origin) of the MSD plot versus time (9) with the following equation:

$$\langle \Delta r^2(t) \rangle = 4Dt + b, \quad \text{[S2]}$$

where b is a variable offset reflecting the spot localization accuracy. To ensure that there was no bias in our tracking analysis, we systematically checked the step length, MSD curves, and mobility histograms for all experiments. The histograms did not show immobile particles, and the averaged MSD curves were predominantly linear, implying Brownian diffusion in all our samples (Fig. S1). In summary, despite the relatively wide distribution of diffusion coefficients obtained by SPT, the median values revealed a clear trend as a function of membrane tension with the overall reduction of the lipid mobility significantly exceeding the experimental uncertainties. Eventually, we plotted the median value and the SE of the diffusion coefficient, as shown in Fig. 2 and Fig. S2.

Role of the Size of the Observation Window in the Analysis of the MSD. The diffusion coefficient of the tracer is extracted from the analysis of the MSD. This diffusion coefficient is typically obtained from the short time behavior of the MSD. Although the MSD appears linear with respect to time at short time, a saturation at larger time is typically observed. In the present experiment, the diffusing protein should experience free diffusion in the fluid membrane; therefore, there should be no confinement effect due to the diffusing medium itself. As a result, we interpret this saturation as the consequence of a truncation of the trajectories compatible with the given observation window. This section provides a theoretical understanding of this effect.

Let us consider that the protein diffuses freely in 2D on a rectangle of dimensions L_x along the x axis and L_y along the y axis. Because diffusion along these two directions is independent, we can relate this problem to the simpler problem of diffusion of a particle in 1D in a finite interval $0 < x < L$.

The conditional probability to be at position x at time t given that the particle left the position x_0 at time 0, namely $P(x,t|x_0)$, obeys the diffusion equation:

$$\frac{\partial P}{\partial t} = D \frac{\partial^2 P}{\partial x^2}. \quad \text{[S3]}$$

When the particle leaves the interval $[0, L]$, we stop observing it, which means that we have absorbing boundary conditions:

$$P(x=0, t|x_0) = P(x=L, t|x_0) = 0. \quad \text{[S4]}$$

Furthermore, we have the following initial condition:

$$P(x, t=0|x_0) = \delta(x - x_0). \quad \text{[S5]}$$

The solution of this problem can be found in the textbook of Doi and Edwards (10) on polymer dynamics, the solution is as follows:

$$P(x, t|x_0) = \frac{2}{L} \sum_{n \geq 0} \sin\left(\frac{n\pi x}{L}\right) \sin\left(\frac{n\pi x_0}{L}\right) \exp\left(-\frac{n^2 \pi^2 t D}{L^2}\right). \quad \text{[S6]}$$

The initial position of the tracer is assumed to be uniformly distributed in the interval so that $P(x_0) = 1/L$ if $0 < x_0 < L$ and zero otherwise. From this, we obtain the probability of the tracer to be at position x at time t as follows:

$$P(x, t) = \int_0^L dx_0 P(x, t|x_0) P(x_0). \quad \text{[S7]}$$

Furthermore, the survival probability, namely, the probability for the tracer to be still in the interval at time t is as follows:

$$P_{surv}(t) = \int_0^L dx P(x, t). \quad \text{[S8]}$$

The MSD conditional on staying in the interval, $\langle \Delta x^2 \rangle_{cond}$, is then the following:

$$\langle \Delta x^2 \rangle_{cond} = \frac{1}{P_{surv}(t)} \int_0^L dx \int_0^L dx_0 (x - x_0)^2 P(x, t|x_0) P(x_0). \quad \text{[S9]}$$

After a bit of calculation, one finds the following:

$$\langle \Delta x^2 \rangle_{cond}(t, L) = \frac{1}{P_{surv}(t)} \frac{4L^2}{\pi^4}$$
$$\times \sum_{n=1}^{\infty} \frac{-4(1 - (-1)^n) - (-1)^n n^2 \pi^2}{n^4} \exp\left(\frac{-D\pi^2 n^2 t}{L^2}\right). \quad \text{[S10]}$$

From this, one obtains the following asymptotic behavior for $t \to \infty$:

$$\langle \Delta x^2 \rangle_{cond} \to L^2 \frac{\pi^2 - 8}{2\pi^2} \simeq 0.0947 L^2. \quad \text{[S11]}$$

For the original problem of diffusion in a 2D rectangular box of dimensions L_x and L_y and a disk of radius R, one obtains the following:

$$\langle \Delta r^2 \rangle_{cond}(t) = \langle \Delta x^2 \rangle_{cond}(t, L_x) + \langle \Delta x^2 \rangle_{cond}(t, L_y), \quad \text{[S12]}$$

which tends asymptotically toward $0.0947(L_x^2 + L_y^2)$, for $t \to \infty$.

It follows from this that one observes a crossover between a linear behavior of the MSD at short times to a constant at long times as illustrated in Fig. S3. The position of this crossover is insensitive to the details of the boundary conditions considered here. In all experiments, we have carefully checked that we were far from the crossover regime when measuring the effective mobility.

Computational Methods. The computational methods follow closely the algorithms developed in ref. 11. The membrane configuration is represented in the Monge gauge as a height function decomposed into Fourier modes above the 2D xy plane. The protein is represented as a location projected to the xy plane. The membrane and protein are coupled mechanically according to the Hamiltonian and hydrodynamic coupling tensor discuss in the main text. The membrane–protein system were thermalized by introducing stochastic driving fields for both the proteins and membrane. The stochastic dynamics were integrated in time using the Euler–Maruyama method (12). A key feature of the membrane–protein coupling is the use of a coupling kernel function G to avoid explicit boundary conditions. The role of G is to model at a coarse-grained level the range of influence of the protein upon the membrane and this term acts to spread protein forces over a spatial patch of the bilayer. This allows for computational efficiency in treating how a protein locally augments the preferred curvature of the lipid bilayer membrane and also the back force that the membrane exerts on the protein. We use the Peskin δ-function for our coupling kernel along with "phase factor averaging" as illustrated in Fig. S4 and discussed in detail in ref. 11. The membrane profiles compared with theory were extracted from our computational model by allowing for the membrane mechanics to relax to equilibrium for a fixed protein and taking a cross-section through the protein location. To obtain statistics, we used a straightforward Monte Carlo approach where independent trajectories were realized for the protein diffusion subjected to the membrane thermal fluctuations. The membrane diffusivity was estimated by fitting the slope of $\langle \Delta r^2(t) \rangle$ after a sufficiently long relaxation time period so that the MSD slope is constant. This standard procedure was done after a short transient period in all of the simulation trajectories. The tension dependence of the diffusivity was determined from simulations of the membrane–protein system started with a flat membrane and letting the system equilibrate. After equilibration, the MSD was computed and the diffusivity statistics determined by generating several simulation trajectories for each reported tension value. In this manner, both the energy minimizing shape profiles and protein stochastic dynamics were obtained from the computational model.

SI Theory

The diffusion of a single protein on a fluctuating membrane has been previously described theoretically by three closely related approaches (13–15). The main ingredient in all these models is the back action of the protein on the membrane fluctuations, an effect of primary importance to predict quantitatively the drag force exerted on the protein. In these models, it is also assumed that the inclusion couples to the membrane curvature by means of a spontaneous curvature modulus although the details of this coupling vary in each model. In the first model developed by E. Reister-Gottfried et al. (14), a system of coupled Langevin equations describing the motion of the protein and the fluctuations of the membrane is established, from which an effective diffusion coefficient is extracted using a path integral approach. These results have been complemented by numerical simulations, which have also been used in the second approach developed by Naji et al. (13). In this reference, Naji et al. have carried out an extensive numerical study of this problem, which shows that the effective diffusion coefficient of the protein is a smooth decreasing function of the protein spontaneous curvature, of the solvent viscosity, and of the ratio of the protein bending modulus and the membrane bending modulus. The authors also find that their numerical results are well described by a simple analytical expression of the effective diffusion coefficient obtained within an adiabatic approximation. In this adiabatic limit, the membrane adopts a shape that minimizes its energy evaluated at the instantaneous protein position. This result can also be recovered from a third approach using an

operator formalism (15). In this approach, the effective drag force experienced by an inclusion moving at constant velocity is derived in the general case that the embedding medium is described by a classical field that couples linearly to the Hamiltonian of the inclusion. Other possible couplings between the inclusion and the membrane can certainly by considered; however, the simplest case in the membrane context is the one considered, namely, the case where the membrane height field is linearly coupled to the inclusion via the local membrane curvature. In the following, we shall follow these assumptions to account for (*i*) the simulations of Naji et al., in particular the smooth dependence as function of the protein bending modulus; and (*ii*) the experimental results presented in this paper on the diffusion coefficient versus membrane tension.

In this section, we assume that the membrane has no internal structure. In contrast, in the following section, we extend this calculation accounting for the bilayer structure of the membrane and additional dissipation mechanisms within the membrane.

Effective Drag Force of a Diffusing Protein in a Membrane with No Internal Structure. We consider a single protein diffusing on a membrane patch of size L^2. The membrane has a bending modulus κ and a tension Σ; it is described by a height function $h(r)$ in the Monge representation. It is also embedded in a fluid of viscosity η. The small inclusion we consider has a radius a_p and a spontaneous curvature C_p. For geometric reasons, $C_p = \theta/a_p$, where θ is the angle associated with the conical shape of the protein, so that $C_p \simeq 1/a_p$. We recall the Hamiltonian of this system, which contains the familiar Helfrich part and a coupling term linear in curvature:

$$\mathcal{H}_0[h, \mathbf{R}] = \frac{\kappa}{2} \int_{L^2} d^2\mathbf{r} \left[\left(\nabla^2 h \right)^2 + \frac{\Sigma}{\kappa} (\nabla h)^2 - \Theta G(\mathbf{r} - \mathbf{R}) \nabla^2 h \right], \quad \textbf{[S13]}$$

where G is a weight function, which is normalized over the whole membrane patch and which accounts for local deformation of the membrane produced by the embedded protein. The amplitude of this coupling is also quantified by the coupling constant Θ. This Hamiltonian carries with it a cutoff length a, which corresponds to the size of the lipids typically 5 nm. Although a and a_p are distinct, both lengths are numerically close to each other for the type of protein inclusion considered here. Because the last term in Eq. **S13** arises from a constraint of membrane curvature, the coupling constant Θ must scale linearly with the spontaneous curvature modulus C_p.

Our main interest is on the force acting on the inclusion $\bar{\mathbf{f}} = -\nabla_R \mathcal{H}_0[h, \mathbf{R}]$, which is expected to be of the form $\bar{\mathbf{f}} = -\lambda \mathbf{v}$ when the velocity of the inclusion $\mathbf{v}$ is sufficiently small, where λ is the effective drag coefficient of the inclusion. To obtain this quantity, we follow below the approach of V. Démery and co-worker (15). Note that these calculations are carried out at fixed $\mathbf{v}$ but Démery and co-worker have shown that the same result is obtained in the ensemble where the force is fixed. We now switch to coordinates moving with the inclusion so that $h(\mathbf{r}, t) = h(\mathbf{r} - \mathbf{R}, t)$. The membrane equation of motion with these new coordinates reads as follows:

$$\frac{dh}{dt} = \frac{\partial h}{\partial t} - \mathbf{v} \cdot \frac{\partial h(\mathbf{r})}{\partial \mathbf{R}} = -\int d\mathbf{r}' \Lambda(\mathbf{r} - \mathbf{r}') \frac{\partial \mathcal{H}}{\partial h(\mathbf{r}')} + \xi(\mathbf{r}, t), \quad \textbf{[S14]}$$

where $\Lambda(\mathbf{r} - \mathbf{r}')$ denotes the Oseen tensor and $\xi(\mathbf{r}, t)$ is a white noise such that $\langle \xi(\mathbf{r}, t) \rangle = 0$ and

$$\langle \xi(\mathbf{r}, t) \xi(\mathbf{r}', t') \rangle = 2k_B T \delta(t - t') \Lambda(\mathbf{r} - \mathbf{r}'). \quad \textbf{[S15]}$$

In the following, we shall assume that a steady state exists in this moving frame. Implicitly, this means that the relaxation time of

the slowest mode is shorter than the characteristic time of the inclusion, so that for the inclusion the membrane appears at equilibrium, an approximation that we further discuss below. It follows from this adiabatic assumption that one can drop the term containing the partial derivative with respect to time in Eq. S14. Let us now focus on the mean value of the membrane height in such a steady state, which obeys the following:

$$-\mathbf{v} \cdot \frac{\partial \langle h(\mathbf{r}, t) \rangle}{\partial \mathbf{R}} = -\int d\mathbf{r}' \Lambda(\mathbf{r} - \mathbf{r}') \left\langle \frac{\partial \mathcal{H}}{\partial h(\mathbf{r}', t)} \right\rangle, \qquad \textbf{[S16]}$$

Now denoting with a bar the average field $\overline{h}(\mathbf{r}) = \langle h(\mathbf{r}, t) \rangle$ at steady state, and its Fourier transform

$$\overline{h}(\mathbf{k}) = \int d^2 r e^{-i\mathbf{k}\cdot\mathbf{r}} \overline{h}(\mathbf{r}), \qquad \textbf{[S17]}$$

we obtain from Eq. S16 the solution

$$\overline{h}(\mathbf{k}, v) = \frac{-\Theta\kappa\Lambda(\mathbf{k})G(-\mathbf{k})\mathbf{k}^2}{2[-ik_z v + \Lambda(\mathbf{k})(\kappa\mathbf{k}^4 + \Sigma\mathbf{k}^2)]}, \qquad \textbf{[S18]}$$

where $\hat{\mathbf{z}}$ is a normal vector along the direction of motion of the inclusion in the plane of the membrane, $\mathbf{R} = z\hat{\mathbf{z}}$ is the location of the inclusion, and v its velocity in that direction. In addition, $\Lambda(\mathbf{k})$ is the Fourier transform of the Oseen tensor introduced above, namely, $\Lambda(\mathbf{k}) = 1/4\eta|\mathbf{k}|$. The stationary profile corresponds to the value of $\overline{h}(\mathbf{k}, v)$ for $v = 0$, which we denote simply as $\overline{h}(\mathbf{k})$:

$$\overline{h}(\mathbf{k}) = -\frac{\Theta\kappa G(-\mathbf{k})\mathbf{k}^2}{2(\kappa\mathbf{k}^4 + \Sigma\mathbf{k}^2)}. \qquad \textbf{[S19]}$$

The shape in real space of such a membrane is discussed in the next paragraph for some specific choices of the weight function $G(\mathbf{r})$. Note that, in all of the choices considered, we assume an isotropic weight function so that $G(\mathbf{k})$ is only a function of $|\mathbf{k}|$.

We now come back to the force acting on the inclusion:

$$\begin{aligned}\overline{\mathbf{f}} &= -\nabla_R \mathcal{H}_0[h, \mathbf{R}] = -\nabla_z \mathcal{H}_0[h, z\hat{\mathbf{z}}] \\ &= \frac{\Theta\kappa}{2} \int d^2 r \nabla_z G(\mathbf{r} - z\hat{\mathbf{z}}) \nabla^2 \overline{h}(\mathbf{r}, v),\end{aligned} \qquad \textbf{[S20]}$$

which after an integration by parts and a Fourier transform becomes the following:

$$\overline{f} = -\frac{\Theta\kappa}{2(2\pi)^2} \int d^2 k i k_z G(\mathbf{k})\mathbf{k}^2 \overline{h}(\mathbf{k}, v). \qquad \textbf{[S21]}$$

After reporting Eq. S18 into this expression and expanding this result to linear order in v, one indeed finds that $\overline{f} = -\lambda v$, with

$$\lambda = \frac{\kappa^2\Theta^2}{4} \int \frac{d^2 k}{(2\pi)^2} \frac{k_z^2 G(\mathbf{k})k^4}{\Lambda(\mathbf{k})(\kappa\mathbf{k}^4 + \Sigma\mathbf{k}^2)^2}. \qquad \textbf{[S22]}$$

Now, the factor k_z^2 in the equation above can be replaced by $1/2|\mathbf{k}|^2$ due to rotational symmetry of the integrand. The final result can be expressed using Eq. S17 as follows:

$$\lambda = \frac{2\eta}{(2\pi)^2} \int d^2 k |\mathbf{k}|^3 \overline{h}(\mathbf{k})\overline{h}(-\mathbf{k}). \qquad \textbf{[S23]}$$

From such an expression, one recovers for a tensionless membrane, equation 7 of Naji et al. (13), by transforming this integral into a discrete sum over $\mathbf{k}$ modes. Such a result can also be

obtained by consideration of the rate of work done on the system to move the protein with the specific velocity v. The idea of the calculation is to evaluate this power loss from standard hydrodynamics in the adiabatic approximation, then to identify the effective friction from the prefactor in front of v^2, where v is the velocity of the inclusion. Our expression agrees naturally with the calculations of ref. 15. This justifies that the effect discussed in this paper is really dissipation driven.

We would like to discuss now the possible relevance of the membrane fluctuations to this effective friction coefficient. We note that the effective friction coefficient, namely, Eq. S23, does not involve the variance of the height fluctuations, as would be expected in a typical fluctuation-related effect but rather the product of the average steady height field. Furthermore, we also note that the effective friction coefficient, namely, Eq. S23, does not contain an explicit temperature dependence. In other words, the result of this calculation would be the same if the temperature of the membrane fluctuations was zero, at least at this order in the calculation, which means within the adiabatic approximation. These two points indicate that the effect described here is not primarily driven by the thermal fluctuations of the membrane.

Another aspect related to membrane fluctuations is the validity of the adiabatic approximation. This approximation supposes that the characteristic time of the phenomenon that we care about—namely, the protein diffusion—is slow with respect to the characteristic time of the membrane fluctuations. This characteristic time is the membrane relaxation time, which depends on the fluctuations modes in a given patch.

Even at the lowest tension of our experiments of the order of 10^{-7} N/m, this relaxation time is dominated by the tension term for a GUV of radius R. In the quasispherical approximation, the mode n is characterized by the wavevector $k = n/R$, and the relaxation time τ_n is as follows (16):

$$\tau_n = 4\eta R(n\Sigma + \kappa n^3/R^2)^{-1}, \qquad \textbf{[S24]}$$

where, as before, Σ is the membrane tension and κ is the bending modulus. In the conditions of our experiment, we find that the slowest relaxation time (for $n = 2$) is still significantly shorter than the characteristic time for diffusion on a length R, namely $R^2/(D_0 n^2)$. For instance, for a radius of 6 μm, the ratio of membrane relaxation time to diffusion time is ~0.02, and for a radius of 20 μm, it is 0.008. This estimation was made with the lowest possible tension experimentally accessible namely 10^{-7} N/m and the bending modulus corresponding to the experiment and typical radius of the GUV. For higher values of the tension and larger radius of the vesicle, the membrane relaxation time will be even shorter than the diffusion time. Therefore, this justifies that, in our experimental conditions, the adiabatic approximation is well verified even for the slowest modes. Note that this would also be the case in the quasiplanar approximation used in the analysis above.

We now explain how to relate this effective friction coefficient to the diffusion coefficient that is measured experimentally. Due to rotational symmetry of the integrand of Eq. S22, one can replace the factor k_z^2 by $1/2|\mathbf{k}|^2$ and in polar coordinates (θ, k), one has $d^2 k = d\theta k dk$. Thus, the angular integral over θ gives 2π. Using $\Lambda(\mathbf{k}) = 1/4\eta k$, one obtains the following:

$$\lambda = \frac{\kappa^2\Theta^2\eta}{2} \int \frac{k dk}{2\pi} \frac{k^7 G(k)}{(\kappa k^4 + \Sigma k^2)^2}. \qquad \textbf{[S25]}$$

This integral runs from the lowest wavevector, which is of the order of $2\pi/L$, to the highest one, which is $2\pi/a$. We approximate the lowest bound by zero. Then using the change of variable

$k = 2\pi x/a$ and introducing the reduced tension $\sigma = \Sigma a^2/4\pi^2\kappa$, we find that the effective drag coefficient $\lambda(\sigma)$ is as follows:

$$\lambda(\sigma) = \frac{\Theta^2\eta}{2a}W_0(\sigma), \qquad \textbf{[S26]}$$

where

$$W_0(\sigma) = \int_0^1 dx \frac{x^4 G(2\pi x/a)^2}{(x^2 + \sigma)^2}, \qquad \textbf{[S27]}$$

and the function $G(2\pi x/a)$ is the Fourier transform of the weight function evaluated at the wavevector $2\pi x/a$. In the limit of large tension $\sigma \to \infty$ and for any choice of weight function, $W_0 \to 0$. Indeed, a highly tense membrane has negligible fluctuations, and thus no friction contribution due to the membrane fluctuations. The flat configuration represents therefore a reference state, corresponding to the bare friction λ_0, which is predictable using the Saffman–Delbrück model. The dissipation due to the fluid displaced by the deformed membrane near the inclusion comes in addition to the one due to this bare friction. Using the Einstein relation, it follows that $D_0 = k_B T/\lambda_0$ is the bare diffusion coefficient of the protein and that D_0 is an upper bound for the diffusion coefficient $D_{eff} = k_B T/\lambda_{eff}$. With the friction λ_{eff} the sum of the bare friction λ_0 and the friction arising from the membrane fluctuations $\lambda(\sigma)$, Eq. **3** of the main text is recovered.

As expected, the function W_0 is independent of the membrane patch size L due to the assumption $L \gg a$, and as a result D_{eff} is also independent of L. Note that, due to some misprint, a similar expression for D_0/D_{eff}, derived in ref. 14 for the case of a tensionless membrane, contains a wrong additional L^2 factor.

The dependence of D_{eff} with the protein radius a_p, can be obtained if one assumes that the protein shape makes a fixed angle with respect to the membrane so that $C_p \sim 1/a_p$ and that the relation $\Theta = 4C_p\pi a_p^2$ still holds. Then it follows from this that $\Theta \sim a_p$. In the regime where the local membrane deformation is much larger than the protein size $a_p \ll \xi$, the drag will be dominated by the contribution due to the membrane deformation. Therefore, using Eq. **3**, one finds $D_{eff} \sim k_B T a/a_p^2$, which agrees with ref. 15 in this regime. Note that such a result is also compatible with the Stokes–Einstein scaling law in $1/a_p$ obtained in ref. 17, because in this reference there is only one characteristic length for the protein so $a \simeq a_p$.

Explicit Form of the Membrane Profile. The model also predicts the deformation of the membrane near the inclusion, which is computed below when the inclusion velocity is zero $v = 0$. The Fourier transform of the average height is Eq. **S19**. In the particular case where the weight function is a Dirac function, $\tilde{G}(\mathbf{k}) = 1$, the integral defining W_0 (Eq. **S27**) can be calculated analytically with the following result:

$$W_0(\sigma) = \frac{3\sigma + 2}{2(\sigma + 1)} - \frac{3\sigma^{1/2}}{2}\arctan\left(\sigma^{-1/2}\right). \qquad \textbf{[S28]}$$

We note that, in this case, the value at zero tension is $W(0) = 1$. Using Eq. **6** of the main text, one finds that the Fourier transform of the membrane profile is in this case:

$$\bar{h}(\mathbf{k}) = -\frac{\Theta\kappa\mathbf{k}^2}{2(\kappa\mathbf{k}^4 + \Sigma\mathbf{k}^2)}. \qquad \textbf{[S29]}$$

The inverse Fourier transform can be done explicitly using polar coordinates:

$$\bar{h}(\mathbf{r}) = -\int \frac{d^2\mathbf{k}}{(2\pi)^2} e^{i\mathbf{k}\cdot\mathbf{r}} \frac{\Theta\kappa\mathbf{k}^2}{2(\kappa\mathbf{k}^4 + \Sigma\mathbf{k}^2)}, \qquad \textbf{[S30]}$$

$$= -\int \frac{kdk}{4\pi} J_0(kr)\frac{\Theta\kappa}{\kappa k^2 + \Sigma}, \qquad \textbf{[S31]}$$

where J_0 is the J-Bessel function. Naturally, the result has cylindrical symmetry so only depends on $r = |\mathbf{r}|$. After introducing the correlation length $\xi = \sqrt{\kappa/\Sigma}$ of membrane fluctuations, the integral over k leads to a modified Bessel function, and one obtains the following:

$$\bar{h}(\mathbf{r}) = \bar{h}(r) = -\frac{\Theta}{4\pi}K_0\left(\frac{r}{\xi}\right), \qquad \textbf{[S32]}$$

where K_0 is a modified Bessel function. From this expression, we also see that Θ represents in this expression the characteristic height of the membrane deformation.

To improve upon the choice of a Dirac function as weight function, we also used Gaussian functions. More precisely, we have chosen a Gaussian of variance equal to the square of the protein size a_p^2. Although other choices of Gaussian functions are possible, it is physically reasonable that the variance of that function should scale with the protein size and be of that order of magnitude. Furthermore, this choice corresponds to a weight function, which is rather close to the one used in ref. 13. Thus, we used the following:

$$G(\mathbf{r}) = \frac{1}{2\pi a_p^2}\exp\left(-\frac{r^2}{2a_p^2}\right), \qquad \textbf{[S33]}$$

which leads after a 2D Fourier transform to the following:

$$G(\mathbf{k}) = \exp\left(-\mathbf{k}^2 a_p^2/2\right). \qquad \textbf{[S34]}$$

The function $W(\sigma)$ introduced in the main text should thus be given by the following integral:

$$W_0(\sigma) = \int_0^1 dx \frac{x^4 \exp\left(-x^2 a_p^2(2\pi)^2/a^2\right)}{(x^2 + \sigma)^2}, \qquad \textbf{[S35]}$$

which needs to be evaluated numerically.

For the membrane profile with the Gaussian weight function, one needs to evaluate numerically the following integral, which comes from the inverse Fourier transform of $\bar{h}(\mathbf{k})$:

$$\bar{h}(\mathbf{r}) = -\int \frac{d^2\mathbf{k}}{(2\pi)^2} e^{i\mathbf{k}\cdot\mathbf{r}} G(-\mathbf{k})\frac{\Theta\kappa\mathbf{k}^2}{2(\kappa\mathbf{k}^4 + \Sigma\mathbf{k}^2)}, \qquad \textbf{[S36]}$$

$$= -\int \frac{kdk}{4\pi} J_0(kr)\frac{\Theta\kappa\exp(-k^2 a_p^2/2)}{\kappa k^2 + \Sigma}. \qquad \textbf{[S37]}$$

Fig. S6 illustrates the influence of the membrane tension Σ, the coupling coefficient Θ and the protein radius a_p on the membrane profile. At long distance from the protein, all of the curves collapse and tend to $h = 0$ corresponding to a flat membrane in our representation.

Effective Drag Force of a Diffusing Protein in a Membrane with Internal Structure. Several studies of membranes show that the Hamiltonian of Eq. **2** fails to describe typical phenomena such as

budding transitions or tube extractions from vesicles. One reason for this is that such phenomena are intrinsically dynamic and that, in a membrane with internal structure, additional dissipative mechanisms are present and must be considered to model the dynamics correctly. Here, we shall be concerned mainly by extending the description to include the bilayer architecture of the membrane in the problem. To do so, we decorate each leaflet with an additional field representing the lipid density deviation about the equilibrium density, which we call $\rho^{\pm}$. Deviation from the equilibrium density for each layer can be accounted for with the modified Hamiltonian (18):

$$\mathcal{H}[h, \mathbf{R}] = \mathcal{H}_0[h, \mathbf{R}] + \frac{k^m}{2} \int_{L^2} d^2\mathbf{r} \left[(\rho^+ - 2dH)^2 + (\rho^- + 2dH)^2 \right],$$

[S38]

where H represents the mean curvature of the membrane, and k^m is the elastic compression modulus of the 2D fluid within each monolayer. A neutral surface can be defined by the property that bending and stretching are decoupled in energy when deformations are defined with respect to it. The neutral surfaces of each monolayer are placed a distance d from the overall neutral surface of the bilayer.

The coupling between the local membrane shape and the densities become more evident if we introduce the reduced density difference $\rho = (\rho^+ - \rho^-)/2$ and the deviation $\tilde{\rho} = (\rho^+ + \rho^-)/2$ of the mean density from its equilibrium value. In the Monge approximation, the above Hamiltonian takes the following form:

$$\mathcal{H}[h, \mathbf{R}] = \int \frac{d^2\mathbf{k}}{2(2\pi)^2} \left[\left(\kappa \mathbf{k}^4 + \Sigma \mathbf{k}^2 \right) |h(\mathbf{k})|^2 + \kappa \Theta G(\mathbf{k})\mathbf{k}^2 h(\mathbf{k}) \right.$$
$$\left. + 2k^m \left(|\tilde{\rho}(\mathbf{k})|^2 + |\rho(\mathbf{k}) - d\mathbf{k}^2 h(\mathbf{k})|^2 \right) \right].$$

[S39]

Note that the previous Hamiltonian is recovered when $\tilde{\rho}(\mathbf{k}) = 0$ and $\rho(\mathbf{k}) = dh(\mathbf{k})\mathbf{k}^2$. This corresponds to the case where the lipid densities of each monolayer have relaxed to their equilibrium value, bending is in this case controlled by κ. In contrast to that, bending at frozen densities where $\tilde{\rho}(\mathbf{k}) = \rho(\mathbf{k}) = 0$ is controlled by $\tilde{\kappa} = \kappa + 2k^m d^2$.

The density fields of each monolayers satisfy conservation laws and are coupled to the membrane height field via boundary conditions, which express the continuity of stress at each monolayer interface. In addition to the restoring force coming from the membrane elasticity and traction forces coming from the displaced fluid above and below each monolayers, these boundary conditions for the stresses include terms associated with the relative friction between both monolayers, which is controlled by the friction coefficient b and the viscous shear damping within each monolayer controlled by the coefficient μ_m (18).

The coupled equations for the two fields $h(\mathbf{k}, v)$ and $\rho(\mathbf{k}, v)$ now take the following form:

$$-ik_z v h(\mathbf{k}, v) = -\frac{1}{4\eta} \left(\tilde{\kappa} k^3 + \Sigma k \right) h(\mathbf{k}, v)$$
$$+ \frac{k^m d k}{2\eta} \rho(\mathbf{k}, v) - \frac{\kappa \Theta G(\mathbf{k}) k}{4\eta},$$

[S40]

$$-ik_z v \rho(\mathbf{k}, v) = -\frac{k^m \mathbf{k}^2}{(2b + 2\eta k + \mu_m \mathbf{k}^2)} \left(\rho(\mathbf{k}, v) - dh(\mathbf{k}, v)\mathbf{k}^2 \right),$$

[S41]

where $k = |\mathbf{k}|$. One can immediately see from Eq. S41 that, when $v = 0$, $\rho(\mathbf{k}) = dh(\mathbf{k})\mathbf{k}^2$. As mentioned above, this corresponds to

the condition for having relaxed monolayers, in which case the membrane is described by the simple Hamiltonian $\mathcal{H}_0[h, \mathbf{R}]$. In view of this, it is clear that the classical picture of a membrane without internal structure still holds in this case but only for the stationary profile when $v = 0$.

From Eq. S41 but now for $v \neq 0$, one finds that $h(\mathbf{k}, v)$ and $\rho(\mathbf{k}, v)$ are proportional to each other:

$$\rho(\mathbf{k}, v) = \frac{k^m d \mathbf{k}^4 h(\mathbf{k}, v)}{(2b + 2\eta|\mathbf{k}| + \mu_m \mathbf{k}^2)(-ik_z v) + k^m \mathbf{k}^2}.$$

[S42]

Then after plugging this result into Eq. S40, one obtains a closed equation for $h(\mathbf{k}, v)$. Now the force acting on the inclusion is still given by Eq. S21. By expanding this force at small velocities, one finds again the form $\bar{f} = -\lambda v$, with an effective friction coefficient

$$\lambda = \left(\frac{\kappa \Theta}{2} \right)^2 \int \frac{d^2\mathbf{k}}{(2\pi)^2} \frac{2\eta G(\mathbf{k})^2 k^3}{(\kappa \mathbf{k}^2 + \Sigma)^2} (1 + \lambda_1),$$

[S43]

with

$$\lambda_1 = \frac{bd^2 k}{\eta} + d^2 k^2 + \frac{d^2 \mu_m k^3}{2\eta}.$$

[S44]

We note that the friction coefficient takes the form of three independent contributions: the first term, namely, $bd^2 k/\eta$, represents the contribution of the friction between monolayers. The second term, namely, $d^2 k^2$, represents an additional contribution of the hydrodynamic friction in the fluid, which adds to the contribution calculated in Eq. S23 but which should be relevant on smaller length scales than that contribution. The third term, namely, $d^2 \mu_m k^3/2\eta$, represents the contribution of the dissipation within the monolayers, which is controlled by μ_m. At the smallest length scales (largest k) of the order of 1 nm, this contribution dominates, but at somewhat larger length scales of the order of the protein size, there is a crossover to a regime controlled by the friction between monolayers (18). On larger length scales, the contribution of the hydrodynamics in the fluid dominates due to the contribution taken into account in Eq. S23. In the end, one can write as before in terms of reduced tension:

$$\lambda(\sigma) = \frac{\Theta^2 \eta}{2a} \left(W_0(\sigma) + \frac{bd^2}{\eta a} W_1(\sigma) + \frac{d^2}{a^2} W_2(\sigma) + \frac{\mu_m d^2}{2\eta a^3} W_3(\sigma) \right),$$

[S45]

where

$$W_i(\sigma) = \int_0^1 dx \frac{(2\pi)^i x^{4+i} G(2\pi x/a)^2}{(x^2 + \sigma)^2},$$

[S46]

with i = 0, 1, 2 or 3. The effective diffusion coefficient is as follows:

$$\frac{D_0}{D_{eff}} = 1 + \frac{D_0 \lambda(\sigma)}{k_B T}.$$

[S47]

Using well-known estimates for the lipid bilayer relevant parameters $a = 5$ nm, $d = 1$ nm (18), $b = 10^9$ J·s·m^{-4} (19) and $\mu_m = 6 \times 10^{-10}$ J·s·m^{-2} (20), one finds that the relative importance of each effects depends on the dimensionless factors $bd^2/\eta a \simeq 200$, $(d/a)^2 \simeq 0.04$, and $\mu_m d^2/2\eta a^3 \simeq 2$. In view of this, it appears that the monolayer friction plays the largest role in the effective friction of the protein (Eq. S45), and consequently on the experienced mobility (Eq. 3).

Considering these dissipative mechanisms internal to the membrane, we find from D_{eff} versus Σ (Fig. S6) and Eq. **S47**, a lower coupling coefficient $\Theta = 3.4 \times 10^{-8}$ m, corresponding to a $C_p = 0.16$ nm^{-1}. This value is compatible with the previous thermodynamic measurements reported in ref. 4.

SI Simulations: Model for Membranes with Embedded Proteins

We presented a detailed model and computational methods for the coupling of a protein that induces curvature within a membrane in refs. 11 and 13. Here, we assume a less general form for the Hamiltonian and use the reduced model when linearizing the membrane–protein coupling:

$$\mathcal{H} = \frac{\kappa}{2} \int_{L^2} d\mathbf{r} \left[\left(\nabla^2 h\right)^2 + \frac{\Sigma}{\kappa}(\nabla h)^2 \right.$$
$$\left. + G(\mathbf{r} - \mathbf{R})\left(-4C_p \nabla^2 h + 4C_p^2\right) \right].$$

[S48]

This Hamiltonian is the same one as the theoretical Hamiltonian in the main text, except for the last term, $4C_p^2$. However, this last term does not contribute to the forces; hence the two models agree under this reduction of the simulation Hamiltonian. Here, G is composed of $G = A_p \tilde{G}$, where $A_p = 100$ nm^2 is the area of the protein and $\int_{A_i} d\mathbf{r} \tilde{G} = 1$. The comparison of the coefficient in front of $\nabla^2 h$ to the linearized Hamiltonian from the main text gives the relationship $\Theta = 4C_p A_p$. The sign convention simply represents whether the protein induces curvature of the membrane that opens upward or downward, which for our system does not affect in any way the diffusion. The specific form of G used in the numerical simulations is given by $G(\mathbf{r}) = A_p \tilde{G}(\mathbf{r}) = A_p/(\Delta x)^2 \phi(x/\Delta x)\phi(y/\Delta x)$, where ϕ is the Peskin-δ function (Fig. S4A and ref. 21), given by the following:

$$\phi(u) = \frac{1}{16} \begin{cases} 3 - u + \sqrt{1 + 4u - 4u^2} & 0 \leq u \leq 1, \\ 5 - u - \sqrt{-7 + 12u - 4u^2} & 1 \leq u \leq 2, \\ 0 & 2 \leq u. \end{cases}$$

[S49]

For the numerical simulations, we used the procedure in ref. 11 with $M_{supp} = 4$ mesh points under the support of G and performing $N_a = 4$ phase-factor averaging shifts. The size of the support of G is 20 nm in each dimension, and hence the spatial discretization is $\Delta x = 5$ nm not including the phase factor averaging. The total number of modes evolved in time is $M = 27$, and hence the total box size $L = 135$ nm. The time step in the numerical integration of the Langevin equations is $\Delta t = 15.4$ ps. For the stiffness, we use $\kappa = 20\ k_B T$, and for the bare diffusivity, we use $D_0 = 2.5\ \mu m^2/s$. For the curvature, we use $C_p = 0.875$ nm^{-1}, which corresponds to $\Theta = 3.5 \times 10^{-7}$ m. The temperature was taken to be 300 K, and the dynamic fluid viscosity of the solvent was chosen to be 10^{-3} Pa·s. For the sampling of the diffusion coefficient, we ran four simulations consisting of at least $N = 1 \times 10^8$ time steps for each of the sampled tension values.

1. Aimon S, et al. (2011) Functional reconstitution of a voltage-gated potassium channel in giant unilamellar vesicles. *PLoS One* 6(10):e25529.
2. Berthaud A, Manzi J, Pérez J, Mangenot S (2012) Modeling detergent organization around aquaporin-0 using small-angle X-ray scattering. *J Am Chem Soc* 134(24):10080–10088.
3. Rigaud J-L, Levy D, Mosser G, Lambert O (1998) Detergent removal by non-polar polystyrene beads: Applications to membrane protein reconstitution and two-dimensional crystallization. *Eur Biophys J* 27:305–319.
4. Aimon S, et al. (2014) Membrane shape modulates transmembrane protein distribution. *Dev Cell* 28(2):212–218.
5. Domanov YA, et al. (2011) Mobility in geometrically confined membranes. *Proc Natl Acad Sci USA* 108(31):12605–12610.
6. Evans E, Rawicz W (1990) Entropy-driven tension and bending elasticity in condensed-fluid membranes. *Phys Rev Lett* 64(17):2094–2097.
7. Mascalchi P, et al. (2012) Probing the influence of the particle in single particle tracking measurements of lipid diffusion. *Soft Matter* 8:4462–4470.
8. Sergé A, Bertaux N, Rigneault H, Marguet D (2008) Dynamic multiple-target tracing to probe spatiotemporal cartography of cell membranes. *Nat Methods* 5(8):687–694.
9. Wieser S, Schütz GJ (2008) Tracking single molecules in the live cell plasma membrane-do's and don'ts. *Methods* 46(2):131–140.
10. Doi M, Edwards SF (1986) *The Theory of Polymer Dynamics* (Oxford University Press, New York).
11. Sigurdsson JK, Brown FLK, Atzberger PJ (2013) Hybrid continuum-particle method for fluctuating lipid bilayer membranes with diffusing protein inclusions. *J Comput Phys* 252:65–85.
12. Kloeden PE, Platen E (1992) *Numerical Solution of Stochastic Differential Equations* (Springer, Berlin).
13. Naji A, Atzberger PJ, Brown FL (2009) Hybrid elastic and discrete-particle approach to biomembrane dynamics with application to the mobility of curved integral membrane proteins. *Phys Rev Lett* 102(13):138102.
14. Reister-Gottfried E, Leitenberger SM, Seifert U (2010) Diffusing proteins on a fluctuating membrane: Analytical theory and simulations. *Phys Rev E Stat Nonlin Soft Matter Phys* 81:031903.
15. Démery V, Dean DS (2010) Drag forces in classical fields. *Phys Rev Lett* 104(8):080601.
16. Solon J, et al. (2006) Negative tension induced by lipid uptake. *Phys Rev Lett* 97(9):098103.
17. Naji A, Levine AJ, Pincus PA (2007) Corrections to the Saffman-Delbruck mobility for membrane bound proteins. *Biophys J* 93(11):L49–L51.
18. Seifert U (1997) Configurations of fluid membranes and vesicles. *Adv Phys* 46:13–137.
19. Fournier J-B, Khalifat N, Puff N, Angelova MI (2009) Chemically triggered ejection of membrane tubules controlled by intermonolayer friction. *Phys Rev Lett* 102(1):018102.
20. Vaz WLC, Goodsaid-Zalduondo F, Jacobson K (1984) Lateral diffusion of lipids and proteins in bilayer membranes. *FEBS Lett* 174:199–207.
21. Peskin CS (2002) The immersed boundary method. *Acta Numer* 11:479–517.

Fig. S1. Averaged MSD as a function of time, estimated from multiple trajectories exploring a defined region of interest (ROI). *Upper Left Inset* illustrates, at the bottom of a GUV, the ROI of various size considered for the single-QD tracking analysis; the truncated circle corresponds to the boundary of the area explored by QDs within the depth of field of the microscope. Experimental data (symbols) are compared with a model (Eq. **S10**, solid line) that describes a protein freely diffusing in 2D on a rectangle of length L_x and width L_y; reported data: one GUV of radius = 23 μm, $L_x = L_y = 0.98$ μm ($\triangle$), 1.67 μm ($\Diamond$), 2.35 μm (∇), and 3.05 μm ($\bigcirc$). The dashed lines are the asymptotes corresponding to a linear behavior of the MSD at short times, $4D_{eff}t$ with $D_{eff} = 2.0$ μm^2/s, and a constant trend at long time, $0.0947(L_x^2 + L_y^2)$. *Lower Right Inset* is a zoom at short time illustrating that the MSD appears linear with respect to time at short time.

Fig. S2. Histograms of KvAP diffusion coefficients for a series of different tensions. D_{eff} is the median diffusion coefficient obtained from N individual trajectories for a single GUV at a given tension Σ.
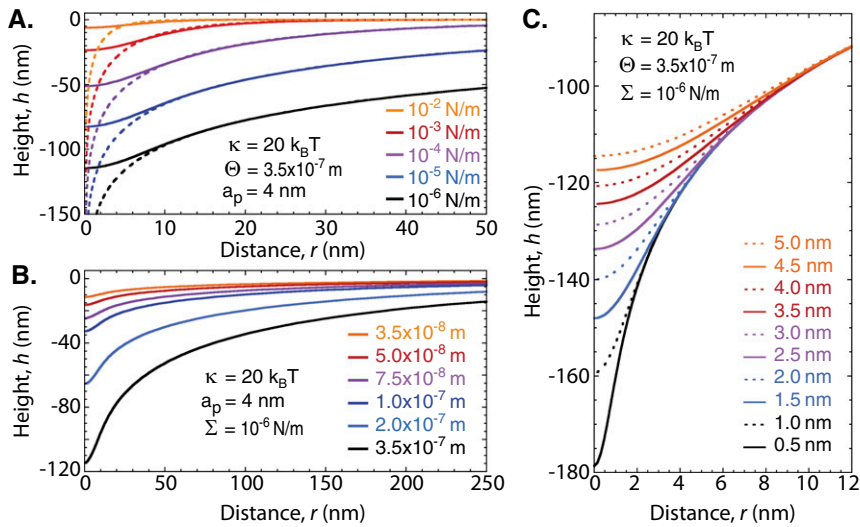
Fig. S3. Membrane shapes calculated from the analytical model using a Gaussian weight (Eq. **S37**) as a function of (*A*) the membrane tension Σ, (*B*) the coupling coefficient Θ, and (*C*) the protein radius a_p. Membrane parameters used for the numerical calculations are reported in *Insets*. The membrane shape determined from a Dirac weight (Eq. **S31**, dashed lines) is also reported in *A* as function of the membrane tension.
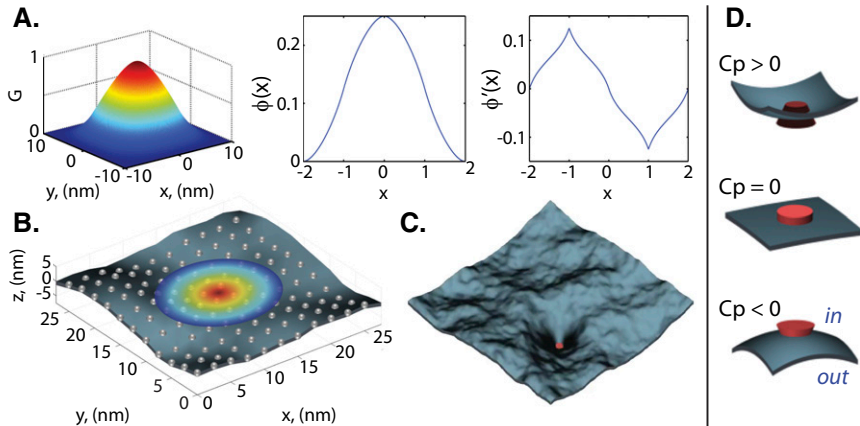

Fig. S4. Illustration of the simulation methodology introduced in refs. 1 and 2. (*A*) The weight function *G* used to couple the membrane and protein in our computations [Peskin-δ function $\phi(x)$ (Eq. **S49**) and of its first derivative $\phi'(x)$]. (*B*) The configuration of the membrane is represented using a discrete Fourier basis with *M* modes in each spatial direction. This is equivalently represented in real space by the values of the height function $h(r)$ sampled on a regular lattice. (*C*) Snapshot extracted from a simulation trajectory showing a typical configuration of the fluctuating membrane and protein during protein diffusion. The protein induces a deformation of the bilayer membrane that is influenced by the membrane tension. (*D*) Proteins may induce different local mean curvatures to the membrane. Shown are the cases associated with the sign of the protein local mean curvature C_p. The inner and outer media of the GUV are shown with "in" and "out."

1. Sigurdsson JK, Brown FLK, Atzberger PJ (2013) Hybrid continuum-particle method for fluctuating lipid bilayer membranes with diffusing protein inclusions. *J Comput Phys* 252:65–85.
2. Naji A, Atzberger PJ, Brown FL (2009) Hybrid elastic and discrete-particle approach to biomembrane dynamics with application to the mobility of curved integral membrane proteins. *Phys Rev Lett* 102(13):138102.

Fig. S5. Semilogarithmic plot of the theoretical diffusion coefficients (D_{eff}) as a function of the membrane tension Σ estimated from Eq. **3** in the main text for different values of Θ and a_p (consequently, D_0). The used parameter values are reported in the table.

Fig. S6. Lipid and protein lateral mobility in fluctuating membranes. Semilogarithmic plot of the diffusion coefficients (D_{eff}) as a function of the membrane tension Σ, for lipids (DSPE, □), for AQP0 (◆), and KvAP (▲) labeled with streptavidin QDs. Each point represents a median diffusion coefficient obtained from hundreds of individual trajectories for a GUV at a given tension; the error bars correspond to SE. KvAP data adjusted by Eq. **S47** (solid line) yields a protein coupling coefficient $\Theta = 3.4 \times 10^{-8}$ m considering $a = 5$ nm, $\kappa = 20$ $k_B T$, $d = 1$ nm, $b = 10^9$ J·s·m^{-4}, $\mu_m = 6 \times 10^{-10}$ J·s·m^{-2}, and $D_0 \simeq 2.5$ µm^2/s.

Movie S1. Simulation of a diffusing protein ($C_p = 0.875$ nm^{-1}, $D_0 = 2.5$ µm2/s) at low tension ($\sum = 5 \times 10^{-5}$ N/m) on a fluctuating membrane (135×135 nm; $\kappa = 20$ $k_B T$). The acquisition interval between frames is 1.54 µs, and the total duration is 617 µs.

[Movie S1](#)

Movie S2. Simulation of a diffusing protein ($C_p = 0.875$ nm^{-1}, $D_0 = 2.5$ µm^2/s) at high tension ($\sum = 5 \times 10^{-3}$ N/m) on a tensed membrane (135 × 135 nm; $\kappa = 20$ $k_B T$). The acquisition interval between frames is 1.54 µs, and the total duration is 617 µs.

[Movie S2](#)